

Magnetic transitions and electrical transport in Bi-doped lanthanum strontium manganites

A.M. Ahmed and H.F. Mohamed

Physics Department, Faculty of Science, Sohag University, Sohag 82524, Egypt
E-mail: fikry_99@yahoo.com

Martin Šoka

Slovak University of Technology, Faculty of Electrical Engineering and Information Technology
Ilkovičova 33, Bratislava 81219, Slovak Republic

Received September 2, 2013

The temperature dependence of the electrical resistivity ρ , thermoelectric power S and the magnetic susceptibility χ of $\text{La}_{0.7-x}\text{Bi}_x\text{Sr}_{0.3}\text{MnO}_3$ ($x = 0.05, 0.10, \text{ and } 0.15$ at.%) manganites were investigated. $\text{La}_{0.7-x}\text{Bi}_x\text{Sr}_{0.3}\text{MnO}_3$ crystallizes in a single phase rhombohedral structure with parasitic phase inclusions. With increasing Bi concentration, a systematic decrease in the ferromagnetic transition temperature (T_C), the metal–semiconducting transition temperature (T_{ms1}) and also the values of activation energies E_p and E_S from $\rho(T)$ and $S(T)$ were observed. On the other hand, in the high-temperature ($T > T_{ms}$) paramagnetic semiconductor regime, the adiabatic small polaron hopping model fit well, thereby indicating that polaron hopping might be responsible for the conduction mechanism. In addition, the thermoelectric power data at low temperatures were analyzed by considering both the magnon and the phonon drag concept, while the high-temperature data were confirmed a small polaron hopping conduction mechanism.

PACS: **71.27.+a** Strongly correlated electron systems; heavy fermions;
75.30.Hx Magnetic impurity interactions;
75.50.Ee Antiferromagnetics.

Keywords: crystal structure, magnetic properties, electrical conductivity, x-ray diffraction, oxides.

1. Introduction

Perovskite-type oxide LAMO (LaAMnO_3 , where A is a divalent alkaline earth metal ion such as Sr^{2+} or Ca^{2+}) exhibits colossal magnetoresistance (CMR) with a magnetic resistance ratio of more than 100% [1–4]. In particular, CMR appears near the point of transition from the antiferromagnetic insulator phase to the ferromagnetic metallic phase, and it is closely associated with Mn in the LAMO specimen having a large spin polarization based on strong Hund’s rule coupling [5]. In this case, the electrical conduction characteristics depend on whether a conduction electron enters an electron orbit in terms of the Jahn–Teller (JT) strain which accompanies the symmetry of the crystal structure [6]. It is known that by doping the bismuth to the system LAMO, the electrical resistivity and magneto-optical effect change [7], but the details are not clear. In order to reveal the mechanism of magneto-transport, Righi *et al.* [8] have investigated the Bi-doping effects on the structural, transport and magnetic properties of $\text{La}_{0.7-x}\text{Bi}_x\text{Sr}_{0.3}\text{MnO}_3$, and have found that the dopant Bi cause structure change

and decreases the T_{ms} . However, interpretation of the temperature dependence of the thermoelectric power (TEP) $S(T)$ for transition metal oxide is rarely reported [9–11] due to the complexity of elucidating the $S(T)$ apart from the diffusion TEP or temperature-independent TEP.

As we know, there are many different properties in $\text{La}_{1-x}\text{Ca}_x\text{MnO}_3$ and $\text{La}_{1-x}\text{Sr}_x\text{MnO}_3$, such as metal–insulator transition temperature at optimal doping and the critical doping concentration for the presence of ferromagnetism [12,13]. So, we have investigated systematically the Bi-doping effect on the magnetic and electrical properties in $\text{La}_{0.7-x}\text{Bi}_x\text{Sr}_{0.3}\text{MnO}_3$ with the expectation that it will provide new insight and interesting physics.

2. Experimental

All samples reported in the present study were synthesized by a standard solid-state reaction procedure. Stoichiometric compositions of $\text{La}_{0.7-x}\text{Bi}_x\text{Sr}_{0.3}\text{MnO}_3$ ($x = 0.05, 0.10, \text{ and } 0.15$ at.%) were prepared by mixing equimolar amounts of La_2O_3 , Bi_2O_3 , SrO , and MnCO_3 , respectively

(all having greater than 99.99% purity). The powders of these oxides and the carbonate were mixed and were finely ground in an electric grinder for 30 min. After grinding, the powders were pressed into pellets with a pressure of 2 ton/cm² and calcined at 1173 K for 8 h followed by cooling to room temperature, they were reground and again pressed into pellets with a pressure of 7 ton/cm² and subsequently calcined at 1373 K for 6 h [14]. Samples were checked by x-ray powder diffraction analysis indicating the presence of a unique phase with perovskite-type structure. Resistivity measurements were performed in a commercial variable temperature liquid nitrogen cryostat. The resistivity was measured as a function of temperature using the standard four-probe method and air-drying conducting silver paste as in previous works [14,15]. The thermoelectric power measurements were carried using the sample two-heater method with copper electrodes see Refs. 15–17. The magnetic susceptibility measurement was performed, from room temperature to 700 K, using the Kappa Bridge KLY-2 with operating frequency 920 Hz.

3. Results and discussion

The x-ray diffraction patterns of the La_{0.7-x}Bi_xSr_{0.3}MnO₃ ($x = 0.05, 0.10, \text{ and } 0.15$ at.%) show that the systematic substitution of La by Bi does not produce relevant effect on them. In general, all the peaks for samples satisfy the La–Sr–Mn–O phase. In addition, some weak impurity peaks from SrMnO, BiSrMnO, and Bi₂O₃ phases were found [14]. The crystal structure for the compositions La_{0.7-x}Bi_xSr_{0.3}MnO_y was found to be rhombohedral structure [18–20]. Lattice parameters and cell volume were calculated and tabulated in Table 1.

As seen in Table 1 the lattice parameter a and unit-cell volume slight increase with increasing Bi concentration, while parameter c slight decreases with x . This almost perfect match can be explained considering the similar dimension of the two cations La³⁺ (ionic radius $r = 1.032$ Å) and Bi³⁺ (ionic radius $r = 1.030$ Å) [21].

Figure 1 shows the variation of resistivity with temperature for La_{0.7-x}Bi_xSr_{0.3}MnO₃. Obviously, the resistivity increases with Bi doping. We expect that when the Bi-content increases not only the La-content decreases but also the charge carrier density [22] which leads to a reduction of the double exchange which is proportional to bandwidth. Therefore, the La/Bi configuration plays a prominent role in controlling the resistivity. Consistently, the figure shows that the transition temperature (T_{ms1}) for

Table 1. The lattice parameters and cell volume (V) with concentration of the La_{0.7-x}Bi_xSr_{0.3}MnO₃

Parameter	Bi content, at.%		
	0.05	0.10	0.15
a , Å	6.043	6.050	6.052
c , Å	7.760	7.760	7.748
V , Å ³	245.41	245.98	245.76

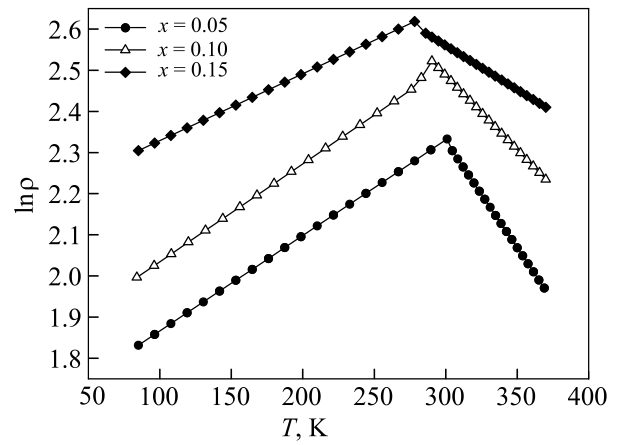


Fig. 1. $\ln \rho$ versus temperature for La_{0.7-x}Bi_xSr_{0.3}MnO₃.

La_{0.7-x}Bi_xSr_{0.3}MnO₃ decreases with increasing Bi content. These compounds have a distinct metallic phase below the transition temperature (T_{ms1}) and above this temperature they become semiconducting (S). In addition both the change in carrier concentration and T_{ms}/T_c with Bi content can be interpreted as arising from the rather covalent character of the Bi–O bonds (which are shorter than the La–O due to the covalent character of the former). That, in turn, contributes to the localization of the oxygen electrons coupling the Mn^{3+/4+} ions, and could explain the increase of the antiferromagnetic interactions and the decrease of the metallic character for the Bi-substituted compounds, ending up with the totally AF and insulating Bi–Sr–MnO₃.

The resistivities data above T_{ms1} (PM–S region) are analyzed in view of small polaron hopping (SPH) are generally used where the transition temperatures of our composites are high temperature. The data are fitted well with the SPH model of Mott [23] viz.,

$$\rho/T = \rho_\alpha \exp(E_p/k_B T), \quad (1)$$

where E_p is the energy equal to $W_D/2 + W_H$; for $T > T_{ms1}$ (where W_H is the polaron hopping energy and W_D is the disorder energy). E_p and ρ_α calculated and tabulated in Table 2. Indeed, as a result of the fit, the adiabatic SPH model is used in the present investigation. As in Table 2 both E_p and ρ_α decrease with increasing Bi content. This behavior is explained by considering that increasing x causes charge delocalization (due to decrease of small

Table 2. The variation of E_p (meV), ρ_α (Ω -cm), E_S (meV), B and W_H (meV) with concentration for $T > T_{ms}$

Parameter	Bi content, at.%		
	0.05	0.10	0.15
ρ_α	6.35	6.33	6.31
E_p	77.50	76.60	76.24
E_S	11.90	9.40	7.50
B	0.035	0.022	0.022
W_H	65.40	67.50	68.74

polaron coupling constant or el–ph interaction constant) in the system and thereby the energy required to liberate a free carrier is reduced.

To discuss the nature of the conduction mechanism below T_{ms1} (FM–M region), the resistivity data are fitted with three empirical equations derived by different previous work [24–26]:

$$\rho = \rho_0 + \rho_2 T^2, \quad (2)$$

$$\rho = \rho_0 + \rho_{2.5} T^{2.5}, \quad (3)$$

$$\rho = \rho_0 + \rho_2 T^2 + \rho_{4.5} T^{4.5}, \quad (4)$$

where ρ_0 represents the resistivity due to grain boundary effects. $\rho_2 T^2$ in term in Eqs. (2) and (4) indicates the resistivity due to electron–electron scattering process and is generally dominant up to 100 K. On the other hand, the term $\rho_{2.5} T^{2.5}$ represents the resistivity due to electron–magnon scattering process in ferromagnetic phase. Finally, the term $\rho_{4.5} T^{4.5}$ indicates the resistivity due to electron–magnon scattering process in ferromagnetic region, which may be likely to arise due to spin-wave scattering process.

Our data of the metallic (ferromagnetic) part of the temperature-dependent resistivity (ρ) curve (below T_{ms}) fits well with Eq. (4) ($R^2 > 99.9\%$). Indicating the importance of grain/domain boundary effects and electron–magnon scattering processes in the conduction of our composites. As in Table 3 the values of $\rho_0 > \rho_2 > \rho_{4.5}$, this means that both grain boundaries and electron–electron scattering process play a role besides an electron–magnon scattering process in conduction mechanism. The last term $\rho_{4.5}$ is also found to decrease with increasing Bi content; the observed behavior may be due to partial alignment of the spins which results in lowering their fluctuations [27].

The temperature dependence of magnetic susceptibility (χ) were measured with a magnetic field of 300 A/m. Figure 2 shows the χ – T curves for $\text{La}_{0.7-x}\text{Bi}_x\text{Sr}_{0.3}\text{MnO}_3$ samples ($x = 0.05, 0.10, \text{ and } 0.15$ at.%), demonstrating the presence of clear FM transitions, while the value of magnetic susceptibility decreases with increasing the doping of Bi for these samples. This phenomenon can be interpreted as the increased bending of the Mn–O–Mn bond with decreasing average A-site ionic radius $\langle r_A \rangle$ due to the partial substitution of smaller Bi^{3+} ions for a bit larger La^{3+} ions. This substitution causes the narrowing of the bandwidth

and the decreasing of the mobility of e_g electron resulting in the weakness of DE interaction magnetism [28] (this confirm the $\rho(T)$ data). Based on these results, ferro- to paramagnetic transition temperatures (T_C) were determined from the inflection point of $d\chi/dT$. It is clear from the values of T_C values are also following the same trend as those of T_{ms} .

Figure 3 shows the dependence of Seebeck coefficient (S) on the temperature. The TEP of these samples, depicted in Fig. 3, is positive at low temperatures, suggesting hole conduction, but becomes negative at high temperatures ($T > 300$ K). The transition from metallic to semiconducting behavior (T_{ms2}) is clearly seen in the figure. Below the T_{ms2} , the value of S increases with increasing Bi doping, above the transition this is also true except for $x = 0.15$ at.%. In addition, above the transition S decreases rapidly. When the resistivity is thermally activated, the thermopower may also be expected to show semiconducting-like behavior. The sign change in S at high temperatures confirms that the coexistence of two types of carriers. The negative S at high temperature is attributed to the electrons which are excited from the valence band (VB) into the conduction band (CB). Because of the higher mobility of electrons within the CB, S is negative. At low temperatures, the electrons in the VB band are excited into the impurity band which generates hole-like carriers, which is responsible for a positive S [29]. The magnitude of S increases with increasing Bi-doping except in the case of $x = 0.15$ above T_{ms2} , and the observed behavior due to the fact that for every ion of Bi doping, double the hole centers, which are localized and causes narrowing of e_g band, this have been confirmed by $\chi(T)$ and $\rho(T)$ measurements.

As in many previous work [30,31] that phonon drag (S_g) and magnon drag (S_m) contributions to the diffusion (S_d) in the low-temperature region. In the low-temperature FM–M region, a magnon drag effect is produced due to the presence of electron–magnon scattering, while the phonon drag is due to electron–phonon scattering. In general, we can analyzed S – T relation as (note that $n_{ph} \sim T^3$, $n_{mag} \sim T^{3/2}$):

$$S = S_0 + S_{3/2} T^{3/2} + S_4 T^4, \quad (5)$$

where S_0 is a constant and accounts the low-temperature variation of thermo-power. The second term $S_{3/2} T^{3/2}$ is attributed to the magnon scattering process, while the origin of the last term $S_4 T^4$ is related to the spin-wave fluctuations in the FM–M region [30]. We fitted our data using

Table 3. The resistivity data, fitted with empirical equations (2)–(4), due to different scattering process

Sample code	$\rho = \rho_0 + \rho_2 T^2$	$\rho = \rho_0 + \rho_{2.5} T^{2.5}$	$\rho = \rho_0 + \rho_2 T^2 + \rho_{4.5} T^{4.5}$	$\rho_0, \Omega\text{-cm}$	$\rho_2, 10^{-5} \Omega\text{-cm/K}^2$	$\rho_{4.5}, 10^{-11} \Omega\text{-cm/K}^{4.5}$
0.05	0.9801	0.9602	0.9977	5.8214	6.6775	1.3144
0.10	0.9921	0.9876	0.9921	7.2756	5.7660	0.0525
0.15	0.9690	0.9466	0.9950	9.4549	7.9799	2.1155

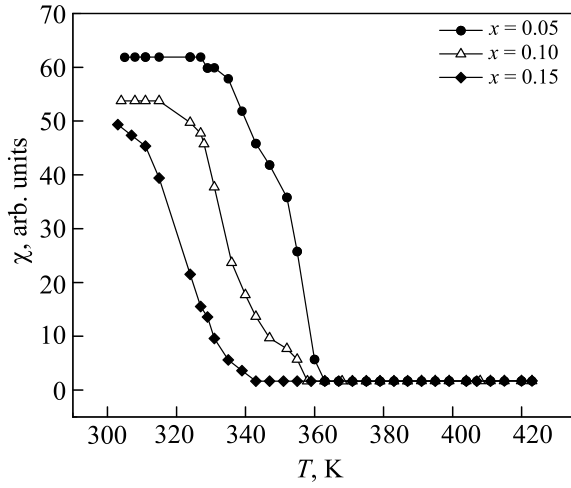


Fig. 2. Temperature dependences of susceptibility for samples $\text{La}_{0.7-x}\text{Bi}_x\text{Sr}_{0.3}\text{MnO}_3$.

Eq. (5) and we found that it fit well only for a short range of low temperature. Therefore, we refit our data using the modified Eq. (6), which modified by adding two more terms, honon drag and diffusion drag and the resulting equation is given by [31]

$$S = S_0 + S_1T + S_{3/2}T^{3/2} + S_3T^3 + S_4T^4, \quad (6)$$

where the term S_1T and S_3T^3 represent to the diffusion and the phonon drag contribution to the TEP, respectively. The lines in Fig. 4, indicate that Eq. (6) is in good agreement with the experimental results of magnon contribution from 83 up to 313, 273, and 263 K high of samples with Bi content $x = 0.05, 0.10$, and 0.15 at.%, respectively. But for the contribution of phonon is in good agreement with experimental results from 163–273, 103–253, and 113–263 K of samples with $x = 0.05, 0.10$, and 0.15 at.%, respectively (Fig. 4(b)). It follows the linear dependence of T^3 through a broad temperature regime and becomes zero at $T = 0$ K. This behavior reflects that the phonon drag effect disappears because the lattice is frozen at $T = 0$ K. Here, it devi-

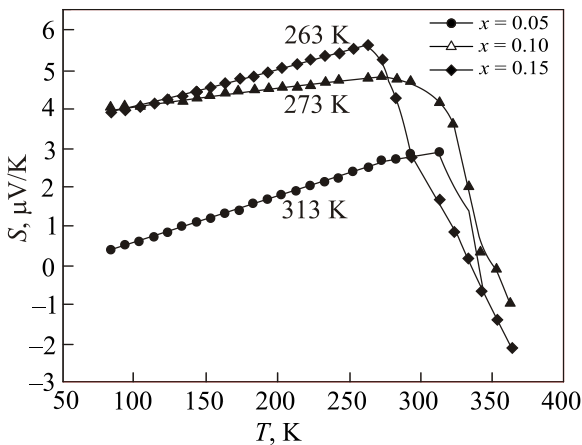


Fig. 3. Temperature dependences of thermoelectric power for $\text{La}_{0.7-x}\text{Bi}_x\text{Sr}_{0.3}\text{MnO}_3$.

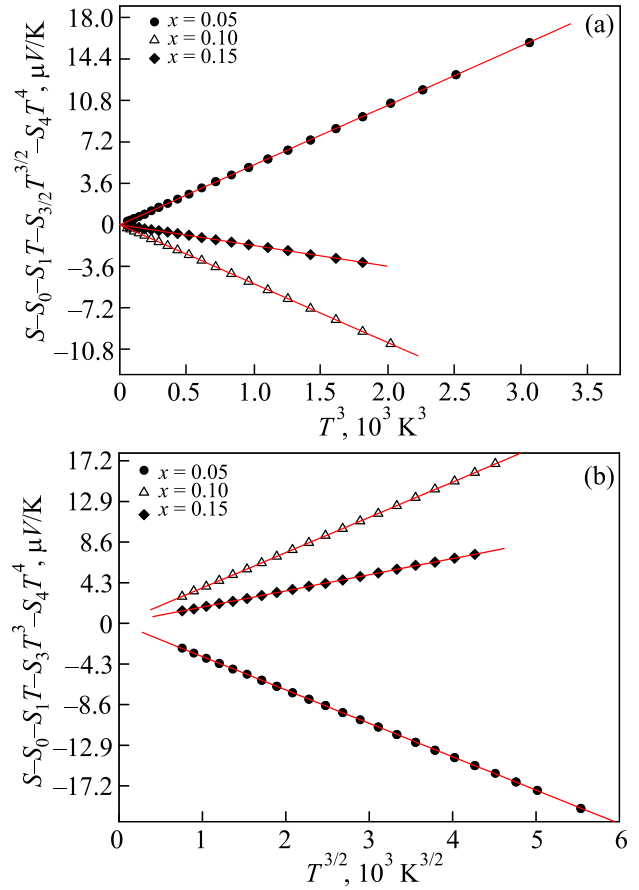


Fig. 4. (Color online) Variations of phonon drag component with T^3 (a) and magnon drag component with $T^{3/2}$ (b). The red lines represent the deviation of linear fit to experimental curve.

ates from the T^3 -dependence below 100 K. The magnon drag component shows $T^{3/2}$ -behavior in several regimes, especially below 173 K. This indicates that the dominant contribution of TEP in low temperature due to magnon drag effect.

The charge carriers in the semiconductor region are not inert and the transport properties are governed by thermally activated carriers because the effect of JT distortions in manganites results in strong electron–phonon coupling and hence the formation of polarons. Therefore, the thermoelectric power data of the present samples in semiconductor regime are fitted to Mott’s polaron hopping equation,

$$S = \pm k_B/e(\Delta E_S/k_B T + B), \quad (7)$$

where k_B is the Boltzmann constant, e is the electronic charge, E_S is the activation energy obtained from thermoelectric power data, and B is a constant. In Eq. (7), $B < 1$ implies the applicability of small polaron hopping model, whereas $B < 2$ indicates the large polaron hopping. From the slope and the intercept of S versus $1/T$ curves (Fig. 5), we obtain the values of activation energy E_S and the constant B (Table 2). The estimated values of B indicated $B < 1$ for three samples. Therefore, the small polaron hopping conduc-

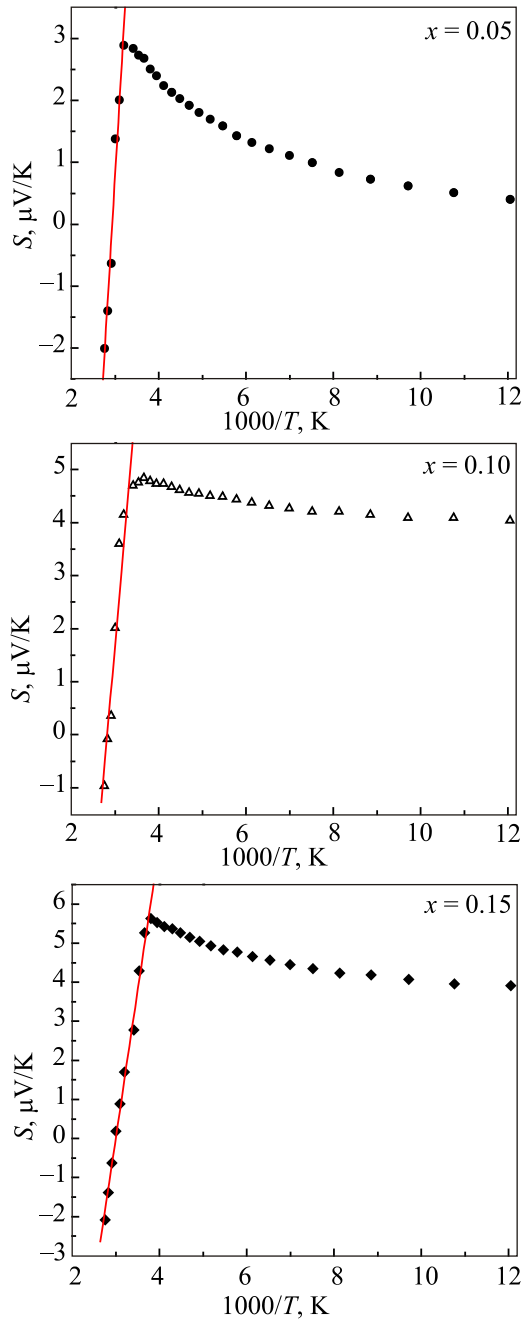


Fig. 5. (Color online) Variations of S vs $1/T$ for samples $\text{La}_{0.7-x}\text{Bi}_x\text{Sr}_{0.3}\text{MnO}_3$. The red lines represent the best fit to SPH model.

tion mechanism is also strongly supported by the high temperature ($T > T_{ms}$) TEP data. From conductivity data also we have approved of the possibility of the formation of small polaron hopping conduction mechanism. Using the activation energy values from $\rho(T)$ plots E_p and those from $S(T)$ plots E_S , the polaron hopping energy values of all the samples have been calculated using the relation, $W_H = E_p - E_S$, and are given in Table 2. The E_p values are found to be higher than those of E_S . Such a large difference in the activation energy is confirm also the applicability of the SPH model in the semiconducting region [30].

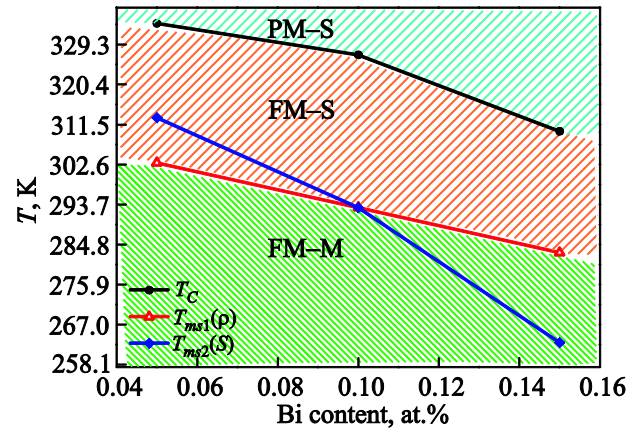


Fig. 6. (Color online) The phase diagram of rhombohedral structure $\text{La}_{0.7-x}\text{Bi}_x\text{Sr}_{0.3}\text{MnO}_3$ ($x = 0.05, 0.10, 0.15$ at.%) system.

The Curie temperature T_C and the metal–semiconducting transition temperatures T_{ms1} and T_{ms2} were deduced from the derivatives of the magnetic susceptibility curves $\rho(T)$ and $S(T)$, respectively. The evolution of T_{ms1} of $\rho(T)$ and T_{ms2} of $S(T)$ and T_C are shown in Fig. 6. This figure shows the phase diagram of rhombohedral structure $\text{La}_{0.7-x}\text{Bi}_x\text{Sr}_{0.3}\text{MnO}_3$ ($x = 0.05, 0.10, 0.15$ at.%) system, where the FM–M phase underlie T_{ms1} (red line), the FM–S phase lie between T_{ms1} (red line) and T_C (black line), finally, PM–S phase lie above T_C (black line).

One interesting feature concerns the value of both T_{ms1} ($\rho(T)$) and T_{ms2} ($S(T)$) which is often smaller than the corresponding value of T_C (about 40 K). These transition temperatures decrease as x increases, as expected. Therefore, we can predict the composition which should lead to the maximum magneto-resistance at the room temperature [32] which is more suitable for applications.

4. Conclusion

In conclusion, temperature-dependent (360–80 K) electrical conductivity and thermopower measurements of the Bi-doped $\text{La}_{0.7-x}\text{Bi}_x\text{Sr}_{0.3}\text{MnO}_3$ ($x = 0.05, 0.10, 0.15$ at.%) system have revealed metal–semiconducting transitions. In other side, the magnetic properties have showed FM–PM transition between 310 and 334 K. The high-temperature conductivity data can be successfully fitted with the small polaron-hopping conduction theory like that of usual oxide semiconductors.

The data of Seebeck coefficient supports the small-polaron hopping transport mechanism. Also, the large difference between E_p and E_S provides evidence of small polaron transport mechanism in the high-temperature PM region.

The metallic state below T_{ms} has been considered in terms of the electron–magnon or electron–phonon scattering process depending on the ambient temperature. From the high difference between the values of T_{ms} and T_C , we predict the maximum magnetoresistance is at room temperature.

Acknowledgments

The authors would like to thank Prof. Dr. Marcel Migliorini and Dr. Marius Pavlovic for they help in susceptibility measurements in Slovak University of Technology, Faculty of Electrical Engineering and Information Technology.

1. Y. Tokura, A. Urushibara, Y. Moritomi, T. Arima, A. Asamitsu, G. Kido, and N. Furukawa, *J. Phys. Soc. Jpn.* **63**, 3931 (1994).
2. Takashi Ogawa, Adarsh Sandhu, Masafumi Chiba, Hiromasa Takeuchi, and Yoshiharu Koizumi, *J. Magn. Magn. Mater.* **290**, 933 (2005).
3. A.M. Ahmed, A. Kattwinkel, K. Bärner, C.P. Yang, J.R. Sun, G.H. Rap, H. Schicketanz, P. Terieff, and I.V. Medvedeva, *J. Magn. Magn. Mater.* **242**, 719 (2002).
4. Elena Rezlescu, Corneliu Doroftei, Paul Dorin Popa, and Nicolae Rezlescu, *J. Magn. Magn. Mater.* **320**, 796 (2008).
5. S. Takemoto, R. Takumi, H. Takeuchi, and Y. Koizumi, *J. Soc. Powder Metall.* **48**, 1107 (2001).
6. L.E. Gontchar, A.E. Nikiforov, and S.E. Popov, *J. Magn. Magn. Mater.* **22**, 175 (2001).
7. T.J.A. Popma and M.G.J. Kamminga, *Solid State Commun.* **17**, 1073 (1975).
8. L. Righi, J. Gutiérrez, and J.M. Barandiarán, *J. Phys.: Condens. Matter* **11**, 2831 (1999).
9. W.H. Jung, *J. Korean Ceram. Soc.* **40**, 849 (2003).
10. P. Mandal, *Phys. Rev. B* **61**, 14675 (2000).
11. S. Bhattacharya, A. Banerjee, S. Pal, R.K. Mukherjee, and B.K. Chaudhuri, *J. Appl. Phys.* **93**, 356 (2003).
12. A.P. Ramirez, S.W. Cheong, and P. Schiffer, *J. Jpn. Phys.* **81**, 5337 (1997).
13. R. Maezono, S. Ishihara, and N. Nagaosa, *Phys. Rev. B* **58**, 11583 (1998).
14. A.M. Ahmed, *Physica B* **352**, 330 (2004).
15. A.M. Ahmed, A.K. Diab, and H.F. Mohamed, *J. Supercond. Nov. Magn.* **24**, 597 (2011).
16. A.M. Ahmed, S.A. Saleh, E.M.M. Ibrahim, and H.F. Mohamed, *J. Magn. Magn. Mater.* **301**, 452 (2006).
17. A.M. Ahmed, S.A. Saleh, E.M.M. Ibrahim, E. Bontempib, and H.F. Mohamed *J. Magn. Magn. Mater.* **320**, L43 (2008).
18. X.J. Fan, J.H. Zhang, X.G. Li, W.B. Wu, J.Y. Wan, T.J. Lee, and H.C. Ku, *J. Phys.: Condens. Matter* **11**, 3141 (1999).
19. S. Uhlenbruck, B. Büchner, R. Gross, A. Freimuth, A. Maria de Leon Guevara, and A. Rvecolevischi, *Phys. Rev. B* **57**, R5571 (1998).
20. A. Pimenov, M. Biberacher, D. Ivannikov, A. Loidl, V.Yu. Ivanov, A.A. Mukhin, and A.M. Balbashov, *Phys. Rev. B* **62**, 5685 (2000).
21. G. Srinivasan, R.M. Savage, V. Suresh Babu, and M.S. Seehra, *J. Magn. Magn. Mater.* **168**, 1 (1997).
22. G.H. Rao, J.R. Sun, A. Kattwinkel, L. Haupt, K. Bärner, E. Schmitt, and E. Gmelinn, *Physica B* **269**, 379 (1999).
23. N.F. Mott and E.A. Davis, in *Electronics Process in Non-Crystalline Materials*, Clarendon, Oxford (1971).
24. A. Banerjee, S. Pal, and B.K. Chaudhuri, *J. Chem. Phys.* **115**, 1550 (2001).
25. L. Pi, L. Zhang, and Y. Zhang, *Phys. Rev. B* **61**, 8917 (2000).
26. G. Jeffrey Snyder, R. Hiskes, S. Dicarolis, M.R. Beasley, and T.H. Geballe, *Phys. Rev. B* **53**, 14434 (1996).
27. V. Ravindranath, M.S. Ramachandra Rao, G. Rangar-ajan, Yafeng Lu, J. Klein, R. Klingeler, S. Uhlenbruck, B. Buchner, and R. Gross, *Phys. Rev. B* **63**, 184434 (2001).
28. J.B. Torrance, P. Lacorre, and A.I. Nazzal, *Phys. Rev. B* **45**, 8209 (1992).
29. J. Yang, Y.P. Sun, W.H. Song, and Y.P. Lee, *J. Appl. Phys.* **100**, 123701 (2006).
30. S. Battacharya, S. Pal, A. Banerjee, H.D. Yang, and B.K. Chaudhuri, *J. Chem. Phys.* **119**, 3972 (2003).
31. B.H. Kim, J.S. Kim, T.H. Park, D.S. Le, and Y.W. Park, *J. Appl. Phys.* **103**, 113717 (2008).
32. G. Srinivasan and D. Hanna, *Appl. Phys. Lett.* **79**, 641 (2001).
- 33.